Influence of Impurity on the Properties of Chemically Synthesized Calcium Hydroxide

Harish[1*], Pushpendra Kumar[1†], Jyoti Kumari[1], Priyanka Phalswal[2], Pawan K. Khanna[2], Amena Salim[3], Rahul Singhal[3], Anoop Kumar Mukhopadhyay[1], Rajendra P. Joshi[4]

[1] *Department of Physics, Manipal University Jaipur, Jaipur-303007, Rajasthan, India*
[2] *Nano-chemistry Lab, Department of Applied Chemistry, DIAT, Girinagar, Pune 411025, India*
[3] *Department of Physics, Malaviya National Institute of Technology, Jaipur-302017, India*
[4] *RI Instruments and Innovation India, Haldwani, 263139, Uttarakhand, India*

Here we report synthesis and characterization of chemically synthesized calcium hydroxide ($Ca(OH)_2$) with and without deliberate presence of $NaNO_3$ as an impurity. Calcium nitrate tetrahydrate ($Ca(NO_3)_2.4H_2O$) is used as precursor and alkaline NaOH solution is used as precipitant to synthesize the $Ca(OH)_2$ samples. The samples were characterized by XRD, FESEM, FTIR spectroscopy, DTA, TGA and UV-Vis spectroscopy techniques. From the UV-Vis spectroscopy results, it is found that the $Ca(OH)_2$ with $NaNO_3$ impurity has higher bandgap than the sample without $NaNO_3$. The weight loss in TGA is also more for the $Ca(OH)_2$ with impurity than the one for without impurity. The results are discussed in terms of composition formed during synthesis process.

Keywords: Calcium hydroxide, NaOH, $NaNO_3$, TGA-DTA, Impurity, Chemical synthesis.

1. INTRODUCTION

Calcium hydroxide is represented as $Ca(OH)_2$. It is an odorless white colored ceramic hydroxide. It is non-toxic and biocompatible in nature. It is usually used in dentistry, industries, agriculture, and biomedical applications. Some other applications of calcium hydroxide include thermochemical heat storage [1, 2]. It is noted that the semipermeable encapsulation of calcium hydroxide can be used for thermochemical heat storage by using the micrometer sized particles [1]. It is also used for cultural heritage conservation [3, 4], network structure development [5], and bone restoration [6]. It is also an important material for Portland cement production and hardening [7, 8]. Other researchers also reported on the effect of the surface area of $Ca(OH)_2$ nanoparticles, on the carbonation kinetics for material construction; environmental and art preservation applications [9]. For all such advanced applications [1-9], the purity of the material matters a lot. If there is an impurity present in the given material, it will have a different electronic structure. This different structure will act as a perturbance factor for the original electronic structure of the phase pure material. Further, the impurity material will have elastic moduli values; different than that of the basic material. As a result, there will be elastic mismatch stress developed in the material due to the presence of impurity. The consequent elastic mismatch strain will try, to distort the lattice. Therefore, the electronic structure will be affected. Hence, there is a genuine chance that the optical band gap may be affected. For instance, the studies on magnesium nitrate impurity in the contribution of NO_x emissions during the thermal decomposition of the solar salt for thermal energy storage; has been reported [10]. As mentioned earlier, one of the most potential material for thermochemical heat storage is $Ca(OH)_2/CaO$ [1, 11]. Stress induced change in band gap is also reported in literature [12]. However, despite having great potential for application of $Ca(OH)_2$ in thermochemical heat storage application; the effect of impurity, that might affect material properties and might produce harmful biproduct; has not been studied in any significant details yet. Hence, we report here the effect of sodium nitrate impurity on the structural, morphological, surface functional, thermal, and optical properties of calcium hydroxide.

2. EXPERIMENTAL DETAILS

2.1 Materials

The chemical precipitation method was used to synthesize calcium hydroxide at room temperature. Calcium nitrate tetrahydrate ($Ca(NO_3)_2.4H_2O$) and sodium hydroxide (NaOH) pro analysis products of analytical grades (Merck, Bengaluru, India) were used in the process. All chemicals were used in the as received condition. First, an aqueous solution of 3M $Ca(NO_3)_2.4H_2O$ was prepared. Next, another aqueous solution of 3M NaOH was also prepared. Both the solutions had 100 ml volume. Here, the $Ca(NO_3)_2.4H_2O$ solution was used as a precursor. Further, the NaOH solution was used as a precipitator. The precipitator was added dropwise into the solution of $Ca(NO_3)_2.4H_2O$. The whole process was carried out under continuous stirring at the rate of 1200 rpm at room temperature. The following reaction results in the formation of calcium hydroxide:

$$Ca(NO_3)_2.4H_2O + 2NaOH \longrightarrow Ca(OH)_2 + 2NaNO_3 + 4H_2O$$

_____

* harishsantoriya@gmail.com
† pushpendra.kumar@jaipur.manipal.edu

After about half an hour, the white precipitate of $Ca(OH)_2$ was obtained. The precipitate was filtered using a Whatman 40 filter paper (GE Healthcare UK Limited, Little Chalfont, Buckinghamshire, UK). Thus, following the method described above, two sample powders A and B were prepared in the present work.

In sample A, the precipitate was washed several times with deionized water to remove trace amount of sodium nitrate ($NaNO_3$) which might have been accidentally present in the precipitated calcium hydroxide powders. These powders were then heated at 60 °C for 2 h in air. The temperature was raised to 60 °C very slowly e.g., at the rate of 1°C/min by keeping the sample in an automatic programmable furnace.

However, in the sample B; the washing of the precipitate with deionized water was *deliberately* avoided. Thus, deliberately the presence of trace amounts of ($NaNO_3$) was preserved in the sample powder B. Therefore, without washing the precipitate; it was directly but very slowly heated to 60 °C for 2 h in air. The heating was done at the rate of 1 °C/min by keeping the sample in an automatic programmable furnace, as was done in the case of the sample A. Then, both the sample powders A and B were characterized by several techniques as detailed below.

2.2 Characterization Techniques

The powder samples A and B were characterized by the XRD, FESEM, FTIR, TGA, DTA, and UV-Vis spectroscopy techniques. The structural phase analysis, crystallite size estimation, and strain evaluation were done for the samples A and B by using the XRD technique. A conventional machine (X'pert pro MPD diffractometer, PANalytical, Almelo, Netherlands) was used for this purpose. The X'Celerator was operated at 40 kV and 30 mA. The XRD data were recorded using CuK_α monochromatic radiation. The characteristic wavelength of the CuK_α radiation was 1.54 Å. The morphological and microstructural details of the samples A and B were studied by the conventional FESEM technique. A standard machine (Supra VP35, Carl Zeiss, Germany) was used for this purpose. In addition, a FTIR spectrometer (JASCO FT IR 460+ Spectrophotometer, Easton, MD, USA) with resolution of 4 cm^{-1} was used to identify the presence of the various chemical bonds and functional groups; present in the surfaces of the samples A and B. The data were recorded for the pertinent wavenumber range of 500-4000 cm^{-1}. The studies on thermally induced phase changes and dissociation processes i.e., the TGA and DTA of the samples A and B were conducted by using a conventional simultaneous thermal analyzer (Shimadzu DTH 60H, Japan). The experiments were conducted from room temperature to 800 °C in air. In both TGA and DTA studies, the heating rates of 10 °C/min were utilized. For all the optical characterizations, a conventional spectrophotometer (Shimadzu, UV-NIR 2600, Japan) was used. Both the samples were sequentially dispersed and ultrasonicated for about half an hour before UV-Vis characterizations, to obtain the clear absorption spectra. The UV-Vis spectra were recorded in transmission mode for both the samples. The data were recorded for the wavelength range of 200-800 nm.

Further, the corresponding Tauc's plots were used for the estimation of the optical band gaps.

3. RESULTS AND DISCUSSIONS

3.1 XRD Analysis

The XRD patterns of both the samples A and B are shown in Fig. 1. These patterns match with those of the hexagonal $Ca(OH)_2$ phase with space group p-3 m1 (Space Group No: 164, PDF Card No. 00–004-0733) as the major phase and the rhombohedral calcite ($CaCO_3$) phase with space group R-3C (Space Group No: 167, PDF Card No. 00–005-0586) as the minor one. Both the samples A and B show almost similar peaks. Thus, several peaks corresponding to the planes (0 0 1), (1 0 0), (1 0 1), (1 0 2), (1 1 0), (1 1 1), (2 0 0), (2 0 1), (1 1 2), and (2 0 2); are present in the XRD patterns. This fact indicates that, both of the samples are polycrystalline in nature. Relatively more broadening of peaks is noted for the impure sample, i.e., sample B.
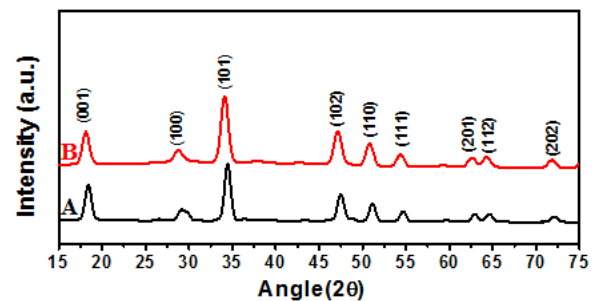
Fig. 1 – XRD patterns of the samples A and B

Therefore, the crystallite sizes (δ) of both the samples A and B are estimated by the well-known Debye-Scherrer (D-S) formula:

$$\delta = k\lambda/(\beta\cdot\cos\theta), \tag{1}$$

where k is a constant of ~ 0.9, λ is wavelength of monochromatic source radiation used to collect the XRD data and β is FWHM (i.e., the full width at half maximum). In addition, θ is the Bragg's angle of diffraction. Thus, the crystallite size (δ) value is estimated to be about 24.5 nm for the sample A. But it drops by more than 50 % to about 10 nm for the sample B. These facts confirm the synthesis of phase pure calcium hydroxide samples with nanoscale crystallite sizes. The smaller crystallite size induces accommodation of more dislocations per unit area. In fact, the corresponding dislocation density (ρ_d) values are therefore estimated as [13]:

$$(\rho_d) = [1/(\delta)^2]. \tag{2}$$

In other words, the number of dislocations is estimated to be ~ ($1.67\cdot10^{15}$ m^{-2}) in the pure sample A. However, in the case of the impure sample B; it jumps by almost an order of magnitude to ~ ($9.99\cdot10^{15}$ m^{-2}). The larger is the number of dislocations stored per unit area, the more becomes the residual strain (ε) in-built in the sample. To test this hypothesis, the size strains due to the nano-crystalline sizes were estimated by the well-known Williamson-Hall method as [13]:

$$\beta\cdot\cos\theta = [\{k\ \lambda/(\delta_{WH})\} + \{(4\varepsilon\ \sin\theta)\}]. \tag{3}$$

Accordingly, the linear fittings of the quantity ($\beta \cos\theta$) as a function of ($\sin\theta$) are done for the samples A and B. Then, from the slopes and intercepts on the horizontal axes of the corresponding linearly fitted lines; the crystallite sizes (δ_{WH}) and the strains (ε) are evaluated. These plots are shown in Fig. 2 (a) and (b) for the samples A and B, respectively. The strain in the sample A is estimated as $\sim (-4.5 \cdot 10^{-4})$. The $-ve$ sign indicates that the strain is compressive in nature. On the other hand, the strain in sample B jumps by almost an order of magnitude to $\sim(-3.2 \cdot 10^{-3})$ although it is still compressive in nature. This increase in strain in the sample B is consistent with its lower crystallite size of about 10 nm as the size strain varies inversely with crystallite size. The presence of the higher strain is most likely to induce more stress in the microstructure of the impure sample B, as compared to that present in the pure sample A. The presence of higher stress in the sample B also corroborates with the size broadening of the corresponding peaks of the sample B as noted earlier, from the XRD pattern shown already in Fig. 1.
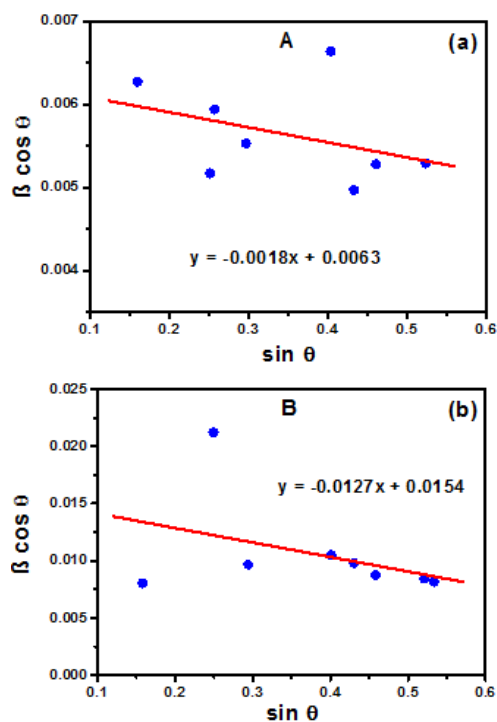
Fig. 2 – W-H plots for the samples (a) A and (b) B

The existence of higher strain is also justified by the presence of an almost order of magnitude higher density of dislocations present in the impure sample B, as compared to that present in the pure sample A. Therefore, the results presented in Fig. 1 and Fig. 2 corroborate well with each other. It is also expected physically that, the presence of even trace amount of $NaNO_3$ should add to existing strain in the hexagonal $Ca(OH)_2$ structure because; the lattice parameters are different.

3.2 Microstructural Study

The microstructure of the pure sample A and the impure sample B are shown in Fig. 3 (a) and Fig. 3 (b),

respectively. It may be seen from the FESEM photomicrograph presented in Fig. 3 (a) that the powders are somewhat agglomerated. In fact, they form clusters. Depending on the extent of agglomeration, the cluster sizes vary from about 10 nm on the lower side to about 500 nm on the higher side. This always happens with nanoparticles. Especially, in the present case of sample A; the crystallite size is fine at about 24.5 nm.
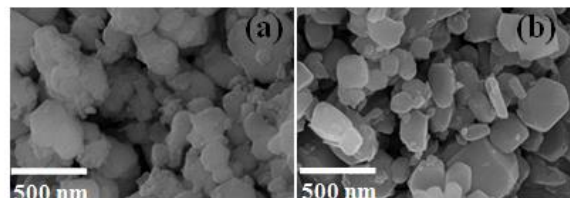
Fig. 3 – FESEM images of the samples (a) A (b) B.

Hence, because of surface charge they have a natural tendency to agglomerate due to Van der Walls interaction. The agglomerating tendency is also guided by the presence of compressive strain. Similar features as of the sample A are also visible in the FESEM photomicrograph 3 (b) for the impure sample B. Only, in this case the finer fraction of nanoparticle clusters is relatively more. This happens because, the sample B has a crystallite size that is lesser than even half of that of the sample A. Hence, there are much more relatively smaller sized agglomerates as compared to those present in the FESEM photomicrograph of the sample A; shown in Fig. 3 (a). Thus, the sample B could agglomerate much more than it is possible with the sample A. This observation is also consistent with the fact that, the strain in sample B is about an order of magnitude higher than that; estimated to be present in the pure sample A. Therefore, these results from the microstructural analysis (Fig. 3) also corroborate well with those (Figs. 1 and 2) obtained from the structural analysis.

3.3 FTIR Spectroscopy Analysis

The FTIR spectra of the samples A and B are shown in Fig. 4. Both of the spectra exhibit a sharp absorption band at 3740 cm^{-1}. It corresponds to the surface -OH group stretching mode. It also indicates the hexagonal structure of $Ca(OH)_2$ present in both the samples A and B. The minor peak at ~ 2400 cm^{-1} corresponds to the atmospheric adsorption stretching of CO_2. Similarly, the broad peak centered at 1500 cm^{-1} shows the $\nu 3$ symmetric stretching of the surface CO_3 group. The similar peaks of $Ca(OH)_2$ are also reported by other researchers [14]. The FTIR spectrum of the sample A shows the characteristics of both hydroxide and carbonate groups of calcium, as expected.

The FTIR spectrum of the sample B also exhibits these characteristics. Further, it exhibits the presence of additional peaks which may be assigned possibly to the presence of impurity. These peaks are only very slightly shifted from the corresponding peak positions of the pure sample A, as expected [14-16]. Classically speaking, for pure $NaNO_3$ the characteristic peaks are scheduled to occur at ~ 1788, 1340-1369 and 835 cm^{-1} due to N=O stretching, NO_3 asymmetric stretching and
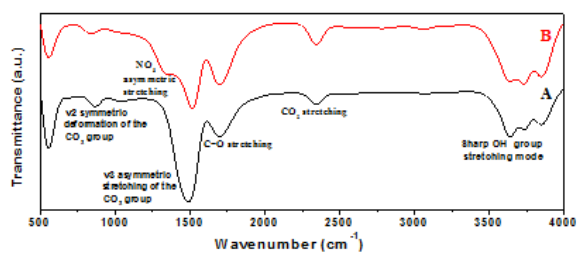
Fig. 4 – The FTIR spectra of the samples A and B

NO_3 symmetric stretching vibrations, respectively [16]. Thus, the peaks present in the FTIR spectrum of the impure sample B at ~ 1698, 1335 and 832 cm^{-1} may be associated respectively with the characteristic N=O stretching, NO_3 asymmetric stretching and NO_3 symmetric stretching vibrations. This happens because, the $NaNO_3$ is present as an impurity in the $Ca(OH)_2$ host. These slight shifts towards the corresponding lower wave numbers happen, due to presence of excess strain in lattice of the sample B and the localized decreases in the relevant force constants [16].

3.4 Thermal Behavior

The TGA-DTA plots for the sample A are shown in Fig. 5(a). Similarly, the DTA-TGA plots for the sample B are shown in Fig. 5(b). The results are discussed sample wise. The weight loss in sample A is about 30 %. It is evident from the corresponding TGA plot, shown in Fig. 5(a). It occurs because, the $Ca(OH)_2$ ceramic decomposes into CaO and water molecules; which get evaporated out of the system [17]. The decomposition process is sharp. It starts at 378 °C and finishes at 450 °C. In accordance, the DTA plot shown in Fig. 5 (a) identifies the endothermic peak position at 442 °C for the pure $Ca(OH)_2$ sample A.

On the other hand, the weight loss in sample B is relatively higher at about 45%. This is evident from the corresponding TGA plot, shown in Fig. 5(b). The DTA of the sample B shows a relatively shallower curve. This happens because of decompositions of both $Ca(OH)_2$ and the impurity. In this case, the decomposition of $NaNO_3$ into $NaNO_2$ and oxygen starts at 450 °C. Thus, the onset of weight loss happens at 450°C and it continues to happen up to 800°C in the sample B, Fig. 5(b).

Other researchers suggest that the decomposition of $NaNO_3$ into $NaNO_2$ and oxygen starts at 600 °C [14]. Therefore, the actual weight loss initiation temperature is in between that (e.g., 378 °C) of $Ca(OH)_2$ and that (e.g., 600 °C) of $NaNO_3$. Hence, this fact reflects the possible formation of a nano/micro scale composite material of $Ca(OH)_2$ and $NaNO_3$.

However, it is obvious from most of the data that this material is more close in terms of structure to the $Ca(OH)_2$ material. Possibly hence, the onset of weight loss initiation temperature is more close to that of the $Ca(OH)_2$ material; rather than to that of the $NaNO_3$ material. Here also, in accordance the DTA plot shown in Fig. 5(b); identifies the endothermic peak position at 498°C for the impure sample B. Clearly, the presence of the trace amount of $NaNO_3$ shifts the endothermic peak position. It is, in fact, higher by about 50 °C as compared to that of the pure sample A. The thermal behaviors of

the samples A and B (Fig. 5) match with the structural (Figs. 1 and 2), morphological (Fig. 3) and FTIR spectroscopy analysis (Fig. 4) data; presented above.
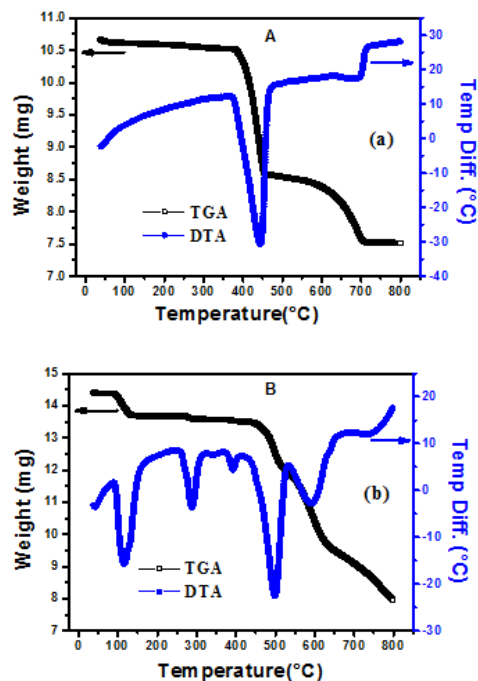
Fig. 5 – TGA-DTA plots of the samples (a) A and (b) B

3.5 Optical Studies

The absorbance spectra of both the samples A and B are shown in Fig. 6. As expected, the impure sample B shows relatively smaller absorbance. The absorbance band edge of sample B also shows a blue shift as compared to that of the sample A. As mentioned earlier, the optical band gaps of the samples were estimated based on these data and the corresponding Tauc plots, shown in Fig. 7 (a, b). Since, $Ca(OH)_2$ is a direct band gap material; the band gap energies (E_g) were calculated using the following relation:

$$(\alpha h \nu)^2 = constant(h \nu - E_g). \qquad (4)$$

Here, α is the absorption coefficient and ($h\nu$) is the energy of the incident photon. From the linear fit of the experimentally measured data (Fig. 7a), the band gap of pure $Ca(OH)_2$ sample A is estimated to be ~ 5.1 eV.
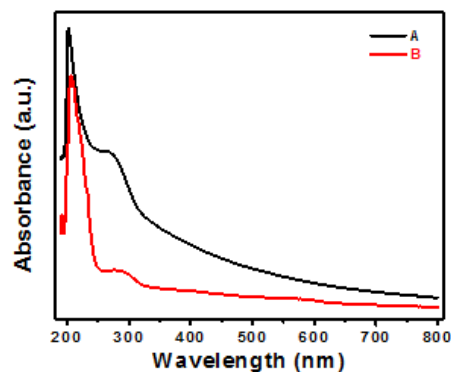
Fig. 6 – The absorbance spectra of the samples A and B

On the other hand, from the linear fit of the stress

corresponding experimentally measured data (Fig. 7b), the band gap of the impure $Ca(OH)_2$ sample B is estimated to be relatively much higher at e.g., ~ 5.4 eV. This is expected to happen because, the sample B possesses higher amount of in-built compressive strain and possibly hence, higher amount of compressive residual stress. Other researchers also noted an increase in band gap due to the presence of residual [12] in the microstructure.
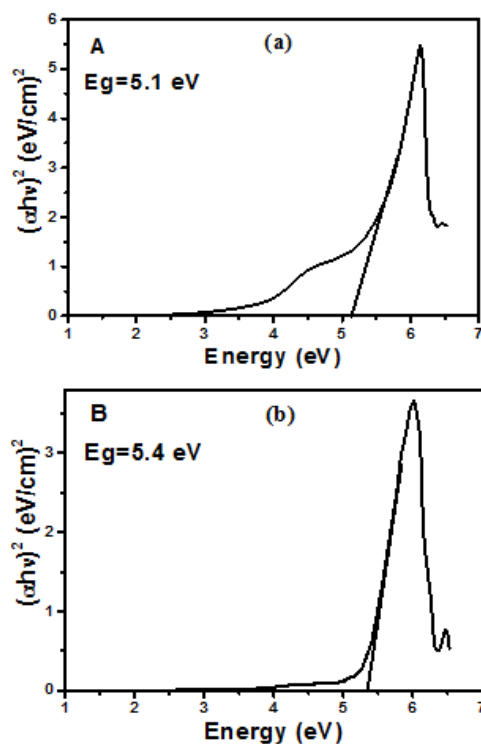
Fig. 7 – Tauc's plots of $(\alpha h\nu)^2$ vs. Energy for the samples (a) A and (b) B

The situation may be physically picturized as follows. The impure sample B bears a blueshift in band edge (Fig. 6). Therefore, the electrons need relatively more energy to first overcome the relatively higher magnitude of the compressive residual stress and then to make the transition across the band gap. In other words, the experimentally measured absorbance data (Fig. 6) and the corresponding estimate of higher band gap in the sample B (Fig. 7b) as compared to that (Fig. 7a) of the sample A; are completely in conformity with each other. Further, these results (Figs. 6 and 7) corroborate well with the results from the structural (Figs. 1 and 2), microstructural (Fig. 3), FTIR spectroscopy (Fig. 4) and thermal behavior (Fig. 5) analyses of the pure $Ca(OH)_2$ sample A and the impure $Ca(OH)_2$ sample B.

4. CONCLUSIONS

The presence of $NaNO_3$ impurity in nanocrystalline $Ca(OH)_2$ leads to reduction in crystallite size as well as enhancements of residual compressive strain, thermally induced weight loss, thermal dissociation temperature, and optical band gap energy. These happen due to the presence of residual compressive stress in the impure sample. The results of the present study could be useful for futuristic design of $Ca(OH)_2$ based nanofunctional materials for thermochemical energy storage in days to come.

ACKNOWLEDGEMENTS

REFERENCES

1. S. Afflerbach, M. Kappes, A. Gipperich, R. Trettin, W. Krumm, *Sol. Energy* **148**, 1 (2017).
2. A. Shkatulov, Y. Aristov, *RSC Adv.* **7**, 42929 (2017).
3. Z. Slizkova, M. Drdácký´, V. Alberto, *J. Cult. Herit.* **16**, 452 (2015).
4. UNI. *Cultural Heritage-Natural and artificial stones- Determination of water absorption by capillarity*, 10859 (2000).
5. S.K. Swain, S. Bhattacharyya, D. Sarkar, *Mater. Res. Bull* **64**, 257 (2015).
6. S.B. Goodman, Z. Yao, M. Keeney, F. Yang, *Biomater.* **34**, 3174 (2013).
7. R.L. Berger, D.S. Cahn, J.D. McGreegor, *J. Am. Ceram. Soc.* **53**, 57 (1970).
8. B.D. Barnes, S. Diamond, W.L. Dolch, *J. Am. Ceram. Soc.* **62**, 21 (1979).
9. R. Camerini, G. Poggi, D. Chelazzi, F. Ridi, R. Giorgi, P. Baglioni, *J. Colloid Interface Sci.* **547**, 370 (2019).
10. C. Prieto, F.J. Ruiz-Cabañas, A. Rodríguez-Sanchez, C.R. Abujas, A.I. Fernández, M. Martínez, E Oró, L.F. Cabeza, *Sol. Energy* **192**, 186 (2019).
11. C. Huang, M. Xu, X. L. Huai, *Heat Transfer Res.* **51**, 1497 (2020).
12. B.C. Mohanty, Y.H. Jo, D.H. Yeon, I.J. Choi, Y.S. Cho, *Appl. Phys. Lett.* **95**, 062103 (2009).
13. R. Vishwaroop, S.N. Mathad, *Sci. Sintering* **52**, 349 (2020).
14. C. Rodriguez-Navarro, A. Suzuki, E. Ruiz-Agudo, *Langmuir* **29**, 11457 (2013).
15. Q. Guo, T. Wang, *Thermochimica Acta* **613**, 66 (2015).
16. M.K. Trivedi, A. Branton, D. Trivedi, G. Nayak, K. Bairwa, S. Jana, *J. Chromatogr. Sep. Tech.* **6**, 1000282 (2015).
17. Harish, P. Kumar, B. Malhotra, P. Phalswal, P.K. Khanna, A. Salim, R. Singhal, A. K. Mukhopadhyay, *Mater. Today: Proc.* **28** No 4, 2305 (2020).